Madden-Julian Oscillation teleconnections to Australian springtime temperature extremes and their prediction in ACCESS-S1

Andrew G. Marshall[1] (ORCID 0000-0003-4902-1462), Guomin Wang[2] (ORCID 0000-0002-1158-2427), Harry H. Hendon[2,3] (ORCID 0000-0002-4378-2263), Hai Lin[4] (ORCID 0000-0003-4353-0426)

1. Bureau of Meteorology, Hobart, Tasmania, Australia
2. Bureau of Meteorology, Melbourne, Victoria, Australia
3. Monash University, Melbourne, Victoria, Australia
4. Environment and Climate Change Canada, Montreal, Quebec, Canada

Corresponding Author: Andrew G. Marshall, Andrew.Marshall@bom.gov.au

Acknowledgements: Support for this work was provided by (i) the Forewarned is Forearmed project (FWFA), which is supported by funding from the Australian Government Department of Agriculture as part of its Rural R&D for Profit programme, and (ii) Meat and Livestock Australia, the Queensland Government through the Drought and Climate Adaptation Program, and the University of Southern Queensland through the Northern Australia Climate Program (NACP). We thank Tim Cowan and Debra Hudson for generously giving their time to help improve the overall quality of this paper. This research was undertaken with the assistance of resources from the National

Computational Infrastructure Australia, a National Collaborative Research Infrastructure Strategy enabled capability supported by the Australian Government.

Abstract

We examine impacts of the Madden-Julian Oscillation (MJO) on Australian springtime temperatures and extremes, explore the mechanisms behind the teleconnections, and assess their prediction in retrospective forecasts using the Bureau of Meteorology's ACCESS-S1 dynamical forecast system. The MJO incites strong and significant warming across southern Australia in phases 2, 3 and 4 when its active convection propagates over the Indian Ocean and Maritime Continent. The heat signal appears strongest in south-eastern Australia during MJO phases 2 and 3 in the vicinity of a deep anticyclonic anomaly which brings warmer airflow to south-western Australia while promoting shortwave radiative heating in the southeast. This occurs as part of a Rossby wave train that emanates from the Indian Ocean and disperses across the Southern Hemisphere along a great circle route towards South America, in response to MJO convective heating on the equator. Importantly, we show the wave train emerges from the divergent outflow from anomalous MJO convection, rather than from the Rossby waves that exist within the MJO's baroclinic structure. Feedbacks between transient eddies and the low frequency flow to the south of Australia and southeast of South America reinforce the wave train in phases 1-3 but act against it during its demise in phase 4. The MJO is a source of subseasonal predictability of springtime heat and cold events over southern Australia in ACCESS-S1 at lead times of 2-4 weeks, yet there remains room for improvement in the model's depiction of the MJO and its teleconnection to the Southern Hemisphere.

Keywords

Madden-Julian Oscillation

Teleconnections

Australia

Temperature extremes

Prediction

ACCESS-S1

1 Introduction

The Madden-Julian Oscillation (MJO; Madden and Julian 1971, 1972) is a well-recognised driver of subseasonal global climate variability. Locally in the tropics, the MJO has been shown to modulate monsoonal activity (e.g., Hendon and Liebmann 1990; Janicot et al. 2011; Lau et al. 2012; Marshall and Hendon 2015; Grimm 2019; Sasikumar et al. 2022), tropical cyclone variability including genesis and track behaviour (e.g., Liebmann et al. 1994; Leroy and Wheeler 2008; Camargo et al. 2009; Ramsay et al. 2012; Klotzbach 2014; Camp et al. 2018), and the development of the El Niño – Southern Oscillation (e.g., McPhaden 1999; Kessler and Kleeman 2000; Bergman et al. 2001; Hendon et al. 2007; Marshall et al. 2009; Marshall et al. 2016). These direct impacts occur via the MJO's circulation anomalies, which resemble the Gill (1980) response to anomalous heating on the equator (e.g., Hendon and Salby 1994; Adames and Wallace 2014). Numerous studies have also demonstrated a remote MJO influence on extratropical weather, climate, and ocean variability and extremes, including rainfall (e.g., Bond and Vecchi 2003; Wheeler et al. 2009; Becker et al. 2011), temperature (e.g., Lin and Brunet 2009; Marshall et al., 2014), fire weather (e.g., Reid et al. 2012; Marshall et al. 2022a), and global ocean surface waves (Marshall et al. 2015). These remote influences occur through atmospheric teleconnections, primarily via excitation of Rossby wave trains (e.g., Hoskins and Karoly 1981; McIntosh and Hendon 2018) that emanate from the tropical Indo-Pacific warm pool region into higher latitudes (e.g., Matthews et al. 2004; Alvarez et al., 2016, Wang and Hendon 2020). Some studies attribute the forcing of wave trains to the advection of planetary vorticity by the divergent outflow from the MJO's equatorial convection (e.g., Mori and Watanabe 2008; Frederiksen and Lin 2013),

while others argue that they rather emanate from the Rossby waves that exist within the MJO's deep baroclinic vertical structure (Adames and Wallace 2014). The discrepancy between these two schools of thought may partly stem from the fact that the former analysis was conducted for austral summer months only, whereas for the latter there was no seasonal separation. Advancing our understanding of these MJO teleconnection pathways is important for their representation in climate prediction systems and, ultimately, for improving subseasonal to seasonal predictions of surface weather and climate (e.g., Lin et al. 2019, 2022).

The MJO affects subseasonal variations in Australia's climate in direct response to its convective anomalies in the tropical north in all seasons except austral winter, and indirectly via tropical-extratropical wave train propagation primarily in winter, spring, and summer (Wheeler et al. 2009; Marshall et al. 2014; Alvarez et al. 2016; Wang and Hendon 2020; Cowan et al. 2022). The wave train in autumn propagates poleward farther to the west than in summer (Alvarez et al. 2016) and influences extratropical Australia to a lesser degree (e.g., Wheeler et al. 2009). A recent study by Marshall et al. (2022b) on the MJO's modulation of Australian temperatures and extremes has shown two of the most pronounced impacts to be (i) daytime warming across the southeast in MJO phases 2 and 3 during spring, and (ii) overnight cooling in the northeast in MJO phases 6 and 7 during winter. Wang and Hendon (2020) recently identified MJO-forced Rossby wave trains as key for driving the latter signal, which results from anomalous equatorward advection of cool and dry continental air and enhanced night-time radiative cooling due to the drier conditions. Here we perform a similar analysis to Wang and Hendon (2020), but for the MJO-induced springtime warming in southeast Australia, to better understand the role of Rossby wave trains in driving the strong extratropical anticyclone in the southeast

Australia – Tasman Sea region that induces this warm signal (Wheeler et al. 2009; Cowan et al. 2022; Marshall et al. 2022b). We also introduce a modelling component to the work by assessing the depiction and prediction of this MJO teleconnection using the Bureau of Meteorology's subseasonal-seasonal prediction system, with a key focus on any enhanced subseasonal predictability of southern Australian springtime heat events afforded by the MJO. Our interest in this teleconnection and its prediction arises from its potential impacts on agriculture, health and emergency services, energy, and fire management, including its possible role in the extreme springtime fire weather conditions in southeast Australia during the devastating and unprecedented Australian bushfire season of 2019-2020 (e.g., Marshall et al. 2022a).

We provide descriptions of the analysis data and methods in Section 2 and introduce the MJO's impact on Australian springtime temperature and extremes in Section 3. Section 4 describes the MJO-forced Rossby wave teleconnection mechanism and the role of mid-latitude eddies in contributing to the signal. In Section 5 we explore subseasonal prediction of the MJO's teleconnection into the Southern Hemisphere, including its role in the prediction of southeast Australian temperature extremes, and we conclude with a summary of key results in Section 6.

2 Data and methods

a) Observed data

We explore the MJO's teleconnections to maximum and minimum temperature extremes across Australia using the Bureau of Meteorology's daily gridded Australian Water Availability Project (AWAP; Jones et al. 2009) data, which are an optimum

interpolation of all available daily station observations (600-800 stations daily) on a 0.25 by 0.25 degree grid. We use the daily gridded European Centre for Medium-Range Weather Forecasts (ECMWF)-Interim reanalysis (ERA-I; Dee et al. 2011) to explore MJO-related variations in horizontal winds, geopotential height, humidity and temperature on standard pressure levels, and downward solar radiation flux at the surface. Streamfunction and the linear S1 Rossby Wave Source (RWS) term (Qin and Robinson 1993) are calculated using the horizontal winds, with the linear S1 RWS depicting the excitation of extratropical Rossby Waves by MJO tropical convective anomalies:

$$S1\ RWS = -\boldsymbol{V}'_{\chi} \cdot \nabla (\overline{\zeta} + f)$$

Here, $\boldsymbol{V}_{\chi}$ is the irrotational wind vector, ζ is the relative vorticity, f is the Coriolis parameter, and the prime and overbar represent the anomaly and mean respectively (see Qin and Robinson 1993, and Wang and Hendon 2020, for more details). We also use ERA-I data for calculating the MJO-forced wave activity flux (WAF; Takaya and Nakamura 2001), which describes the evolution and propagation of quasi-geostrophic stationary Rossby waves on a zonally varying basic flow. We note the caveat that WAF does poorly in the context of breaking Rossby waves, for which quasi-geostrophic theory does not well apply. WAF is shown to be suitable for illustrating Rossby wave train propagation from the tropics to the extratropics on the timescale of the MJO (Wang and Hendon 2020). WAF relates to the RWS in that the divergence of WAF indicates a wave-source region. Finally, we assess MJO-related variations in tropical convection using daily mean interpolated outgoing longwave radiation (OLR)

gridded data from the National Oceanic and Atmospheric Administration (NOAA) (Liebmann and Smith 1996).

We calculate anomalies relative to climatology for all data analysed in this study. Our analysis spans the period 1990-2012 and we compute non-overlapping weekly means for each spring season (September–November) to coincide with our subseasonal forecast model framework (described below). Thirteen samples of weekly means were calculated between 27 August and 19 November each year. The averaging over 1990-2012 for each of the thirteen weeks defines the weekly climatology from which the weekly anomalies were derived.

b) Rotated Madden-Julian Oscillation Indices

We monitor the MJO using the Real-time Multivariate MJO index pair, RMM1 and RMM2, from Wheeler and Hendon (2004). Derived from a combined Empirical Orthogonal Function (EOF) analysis of equatorially averaged outgoing longwave radiation (OLR) and zonal wind at 200 and 850 hPa, these indices capture the eastward-propagating large-scale structure of the MJO in zonal wind and convection along the equator and provide a measure of the amplitude $(=\sqrt{RMM1^2 + RMM2^2})$ and phase $(=\tan^{-1}(RMM2/RMM1)$ of the MJO. A positive RMM1 corresponds to enhanced convection centred over the Maritime Continent (represented by MJO phases 4 and 5; Wheeler and Hendon 2004), and a positive RMM2 represents a convection dipole with an enhanced centre over the western Pacific Ocean and a suppressed centre over the central Indian Ocean (MJO phases 6 and 7). As such, RMM2 lags RMM1 by a quarter of a cycle, or about 10 to 15 days.

We regress the anomaly fields onto the RMM indices to derive composites associated with distinct phases of the MJO (Virts and Wallace 2014). Since the MJO phases that are depicted by RMM1 and RMM2 straddle the original phases defined by Wheeler and Hendon (2004), we adopt the method of Wang and Hendon (2020) and first rotate the axes of RMM1 and RMM2 by $\theta = \pi/8$ to produce better alignment with the original phases:

$$RMM1^* = cos(\theta)RMM1 + sin(\theta)RMM2$$

$$RMM2^* = -sin(\theta)RMM1 + cos(\theta)RMM2$$

Then, following Virts and Wallace (2014), we can depict anomalies that represent MJO phases 5, 6, 7 and 8 by regressing onto the time series of RMM1*, RMM1*+RMM2*, RMM2*, and RMM2*-RMM1*, respectively. The anomalies associated with phases 1, 2, 3 and 4, which are the key focus of this study, are obtained by simply changing the sign. Statistical significance of the regression coefficients is based on Student's (1908) t-test with the effective sample size estimated following Bretherton et al. (1999).

Other MJO indices that could be used for this study are the OLR-based univariate MJO indices (Straub 2013; Kiladis et al. 2014), which also provide useful assessments of MJO variability particularly when the convective signal is of primary interest (Kiladis et al. 2014; Wolding and Maloney 2015, Wang et al. 2018). Although the gross features of MJO convective and circulation anomalies are similar for the RMM and OLR-based indices, there can be differences in the amplitude and phase of individual MJO events from one index to the next (e.g., Kiladis et al. 2014). Thus, we

recognise that the MJO phases presented in this work are specific to our use of the RMM indices.

c) ACCESS-S1 retrospective forecast data

We assess predictability of Australian temperature extremes and the role of the MJO using version 1 of the Australian Community Climate and Earth System Simulator-Seasonal forecast system (ACCESS-S1; Hudson et al. 2017), which replaced the low resolution-low top model POAMA (Alves et al. 2003) to become the Bureau of Meteorology's operational coupled model subseasonal to seasonal prediction system in August 2018. Based on the UK Met Office GC2 coupled model GloSea5 system (MacLachlan et al. 2015), ACCESS-S1 has high spatial resolution with 25 km in the ocean, ~60 km in the atmosphere, and 85 vertical levels in the atmosphere. Retrospective forecast (hindcast) and real time initial conditions for sea-ice and the ocean are provided from the assimilation produced at the UK Met Office (e.g. Mogensen et al. 2009, 2012; Maclachlan et al., 2015). The atmospheric initial conditions for the hindcasts are provided by interpolating zonal wind (u), meridional wind (v), temperature, humidity, and surface pressure from ERA-I onto the ACCESS-S1 atmospheric model grid. In real time, the atmospheric initial conditions are provided by the Bureau of Meteorology Numerical Weather Prediction system. Soil moisture is initialized with climatology (MacLachlan et al. 2015) and soil temperatures are interpolated from ERA-I data.

The ACCESS-S1 subseasonal hindcasts consist of an 11-member ensemble initialized on the 1st, 9th, 17th and 25th of each month during 1990-2012. Ensemble

initial conditions are produced by a simple scheme that adds randomly sampled 7-day differences from ERA-I (rescaled to represent analysis uncertainty) into the atmospheric initial state (Hudson et al. 2017), and model uncertainty is provided by the stochastic backscatter scheme (MacLachlan et al. 2015). We analyse weekly-mean output from the first month of each hindcast at lead times of two, three and four weeks, for the data fields described in Section 2a. Week two is defined as the mean of the second week of each hindcast, week three as the mean of the third week, and week four as the mean of the fourth week. We aggregate the data for the spring season based on the validity/target date, as opposed to the start date, for each week. Hindcast anomalies are formed relative to the hindcast model climatology, which is a function of both start date and lead time, and thus a first-order linear correction for model mean bias is made in a similar fashion to that of Stockdale (1997).

For assessing the MJO in ACCESS-S1, we create predicted RMM1 and RMM2 indices by projecting the model's predicted anomalies of equatorially averaged outgoing longwave radiation and zonal winds at 200 and 850 hPa onto the observed EOF pair (Rashid et al. 2011). Prior to projecting the daily observed and predicted anomalies onto the observed EOF pair, interannual variability is removed by subtracting the previous 120-day mean. For the ACCESS-S1 hindcasts this involves subtracting a 120-day mean that is created for a lead time of τ days as the mean of the previous 120-τ days of observations up to the start of the forecast plus the τ days of the forecast. We use the common practice of removing the previous 120-day mean (Wheeler et al. 2004), rather than a centred 120-day mean (e.g., Lyu et al. 2019), for consistency with MJO monitoring in the ACCESS-S1 operational real-time system, for which a centred running mean filter is not possible due to the lack of information from the future. A comparison of these methods, including caveats concerning the use

253 of the former, is provided by Lyu et al. (2019) and Dr Andrea Jenney[1]. We finally
254 rotate the RMM indices for ACCESS-S1 as we do for observations and regress the
255 hindcast anomalies onto the RMM* combinations described in Section 2b.

256

257 *d) Temperature extremes*

258

259 We define maximum temperature extremes across Australia using the upper
260 quintile (i.e., top 20 percent of climatology) of weekly-mean maximum temperature at
261 each grid point, using the *Occurrence Frequency of Change (OFC)* from Wang and
262 Hendon (2020):

263

264 $$OFC = \frac{\left[\frac{MT_k(x,y)}{N_k} - 0.20\right]}{0.20}$$

265

266 Here, N_k is the number of active MJO events in phase k, $MT_k(x,y)$ is the
267 number of occurrences when maximum temperature exceeds the upper weekly
268 quintile threshold at a grid point (x,y), and 0.20 is the mean quintile probability of
269 occurrence. For a given MJO phase k, an active MJO event is defined when the
270 weekly MJO index amplitude is greater than one (e.g., Wheeler et al. 2009). *OFC*
271 measures to what extent an active MJO event changes the occurrence of weekly
272 maximum temperature to be in the upper quintile. For instance, an *OFC* of 0.5
273 indicates a 50% increase in occurrence as compared to climatology. We conduct a
274 non-parametric resampling test to assess the significance of *OFC*. For this, N_k weekly

[1] https://sites.google.com/ucar.edu/jenney/research/running-mean-filtering

values are randomly selected without replacement 2000 times to establish the 5% and 95% confidence intervals for the null hypothesis that there is no change in *OFC* for a given MJO phase. Changes in *OFC* are thus deemed to be significant when the composite *OFC* values fall outside this range.

3 MJO impact on springtime temperature and extremes over Australia

The typical springtime responses of weekly mean maximum and minimum temperature associated with MJO phases 1, 2, 3 and 4 are displayed in Fig. 1. We highlight these four phases due to their known impacts on extreme daytime heat (Marshall et al. 2014; Marshall et al. 2022b) and fire weather (Marshall et al. 2022a) over south-eastern Australia during spring. We also note that the responses for the other four MJO phases are equal and opposite in sign. For display, the regression coefficients are scaled for an MJO amplitude of 1.5 standardized units, which is approximately the mean MJO amplitude for all times when the amplitude is greater than one. Strong and significant increases occur in MJO phases 2, 3 and 4 over the southeast for maximum temperature (Fig. 1a) and minimum temperature (Fig. 1b), while moderate increases occur in MJO phase 1 over southern Australia for maximum temperature and mostly the southwest for minimum temperature. The anomalous warming is overall stronger during the day than during the night, especially in phases 2 and 3 when the regression coefficients for maximum temperature are around twice those for minimum temperature.

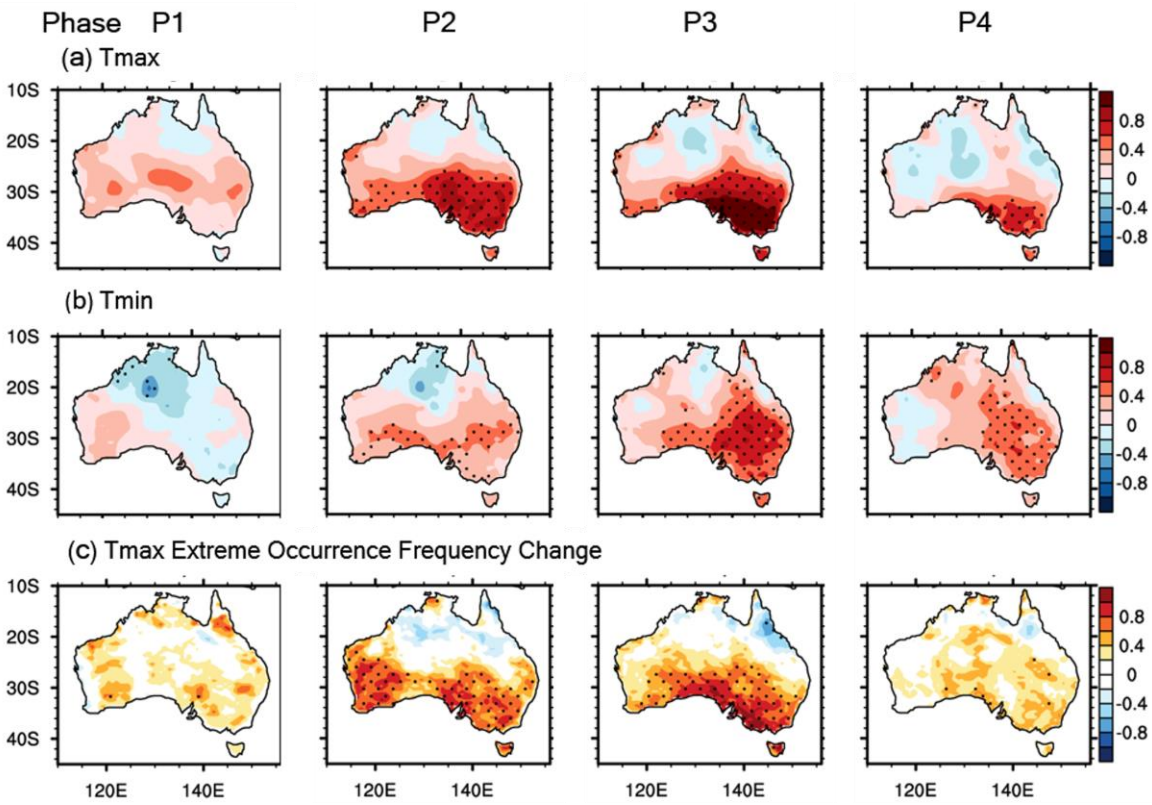

Fig. 1 Regression of Australian (a) maximum temperature and (b) minimum temperature anomalies onto the MJO indices for phase 1 to 4 (left to right). Regression for the other four MJO phases are identical but opposite in sign. The regression coefficients are scaled for an MJO amplitude of 1.5. Shading interval is 0.2 ºC. Dots indicate where regression coefficients are significant at $p < 0.05$ based on Student's (1908) t-test. (c) Maximum temperature extreme event *Occurrence Frequency Change (OFC)* as defined in Section 2. Shading interval is 0.2. Dots indicate significant differences from zero at $p < 0.05$ based on a resampling test as described in text.

The MJO's impact on weekly maximum temperature extremes is quantified by the *OFC* in Fig. 1c. The likelihood of being in the highest quintile greatly increases over southern Australia in MJO phases 2 and 3, with *OFC* values of 0.5 to 1.0 indicating an increase in occurrence of 50-100% as compared to climatology. Put another way, the likelihood increases from 20% in the mean to 30-40% in these

phases (i.e., 1.5 to 2 times more likely). These values peak over parts of the southeast in phase 2, and coastal parts of the south in phase 3, coincident with the regions of maximum warming in Fig. 1a. Interestingly, the MJO's impact on southwest Western Australia in phase 2 appears more pronounced for *OFC* (Fig. 1c) than for anomalous daytime temperature (Fig. 1a), suggesting a greater MJO influence on the upper tail of the maximum temperature distribution than on the mean in this case. MJO phases 1 and 4 also show increases in the occurrence of extreme daytime heat, however the impacts appear less concentrated in the south and more modest in magnitude overall, with *OFC* values ranging 0.2 to 0.5 over large parts of the country.

Previous work has shown MJO phases 2 and 3 in spring to be characterized by a strong anticyclonic anomaly over southeast Australia and the Tasman Sea in association with a mid-latitude wave train (Wheeler et al. 2009). This leads to suppressed rainfall over much of southeast Australia, although the teleconnection has weakened somewhat since 2009 particularly over Victoria and Tasmania in phase 3 (Cowan et al. 2022). We expand on the work of Wheeler et al. (2009) to elucidate the MJO teleconnection to strong springtime warming over southern Australia (Fig. 1). With a focus on MJO phase 2, for which the MJO-induced anticyclonic anomaly near southeast Australia has strengthened and expanded over the Tasman Sea in the last 15 years (Cowan et al. 2022), we examine circulation anomalies at 200 hPa (Fig. 2a) and 850 hPa (Fig. 2b), surface shortwave radiation flux anomalies (Fig. 2c), and temperature tendency at 850 hPa (Fig. 2d). The latter is the rate of change of anomalous temperature $\partial T'/\partial t$ (in units of °C per day) due to horizontal advection, derived from the temperature advection equation:

337 $$\frac{\partial T'}{\partial t} = \boldsymbol{v}' \cdot \nabla \bar{T} + \bar{\boldsymbol{v}} \cdot \nabla T' + \overline{\boldsymbol{v}' \cdot \nabla T'}$$

338

339 The first term on the right-hand side represents anomalous advection of the
340 mean temperature gradient, the second term represents mean advection of the
341 anomalous temperature gradient, and the third term – the time mean of the anomalies
342 – is negligible.

343

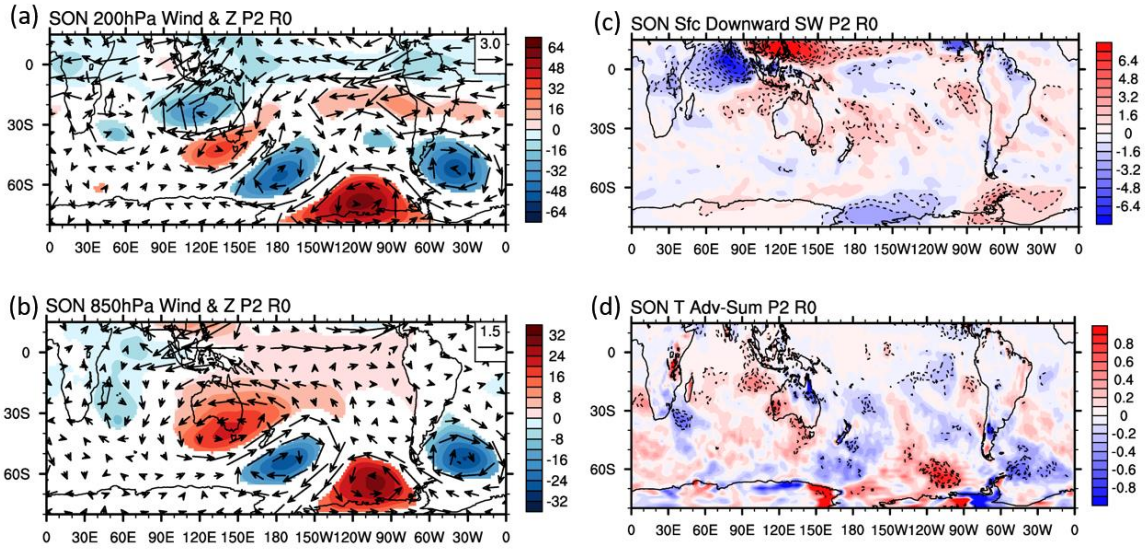

344

345 **Fig. 2** MJO phase 2 regression for geopotential height and horizontal wind anomalies at (a)
346 200 hPa and (b) 850 hPa (vector scale m s^{-1} in upper right; geopotential height shaded (m)
347 only shown where significant at $p < 0.05$); (c) downward solar radiation flux anomalies at the
348 surface (shading interval 0.8 W m^{-2}, positive means a heating of the surface atmosphere) and
349 (d) temperature tendency anomalies at 850 hPa due to horizontal advection (shading interval
350 0.1 ^{o}C day^{-1}). In (c) and (d) dashed contours indicate significant anomalies at $p < 0.05$.

The increases in maximum and minimum temperature over southern Australia occur in the vicinity of an upper-level anticyclonic anomaly that is centred to the west of Tasmania, and to the south of an upper-level cyclonic anomaly that is centred off the central Western Australian coast, where the anomalous flow is easterly (Fig. 2a). The increase in mid-tropospheric geopotential height and anticyclonic flow over southeast Australia (Wheeler et al. 2009) extends across the continent in the lower levels, bringing anomalous easterly and north-easterly wind flow to the south (Fig. 2b). This circulation forms part of a tropical-extratropical wave train comprising positive–negative geopotential height anomalies; these emanate towards the southeast from the equatorial eastern Indian Ocean region, where the low-level flow resembles the Gill (1980) response to a tropical heating anomaly centred near 70-80°E (see Fig. 4 for the location of the MJO convective anomalies in phase 2), to the high latitudes near South America.

The easterly and northeasterly low-level anomalies over southern Australia would act to advect warmer continental air, thus driving warmer daytime and overnight conditions across the south. We particularly note the importance of advection for building up heat in southwest Western Australia, which is reflected in the strong positive temperature tendency at low levels (Fig. 2d). Meanwhile, the anomalous anticyclonic high and associated lack of rainfall over south-eastern Australia (Wheeler et al. 2009) gives rise to an increase in (downward) shortwave radiation at the surface (Fig. 2c), which also promotes daytime warming in the southeast. Together, this pattern of circulation and shortwave anomalies suggests that increased temperatures in the southwest are primarily driven by advection of warm air across southern Australia, while the local peak in daytime warming in the southeast

(Fig. 1a) is largely influenced by enhanced solar radiation at the surface. Indeed, near-zero anomalies can be seen in downward shortwave radiation over the southwest (Fig. 2c) and in the advection-driven temperature tendency over the southeast (Fig. 2d).

We elucidate the MJO's impact on upper- and lower-level circulation anomalies with a simple linear model that responds to tropical heating anomalies characteristic of MJO convection, under a SON basic state. The model used is the simplified primitive-equation atmospheric general circulation model (SGCM) as introduced in Hall (2000), which is run at triangular 31 horizontal resolution and 10 vertical levels. The linear integration of SGCM is performed with the approach as described in Hall and Derome (2000) and Lin et al. (2010). This idealised forcing experiment prescribes MJO-scale heating and cooling anomalies, centred on 70°E, 7.5°N and 140°E, 10°N respectively, to mimic the enhanced and suppressed convective anomalies of the MJO in phase 2 during SON (e.g., Wheeler et al. 2009), and runs for 20 days after the forcing is switched on. The thermal forcing has an elliptical form in the horizontal and a vertical profile of $(1 - \sigma)\sin[\pi(1 - \sigma)]$, which peaks at $\sigma = 0.35$ with a vertically averaged heating rate at the centre of 2.5 K day^{-1}. Fig. 3 shows the anomalous responses in geopotential height at 200 hPa and 850 hPa at three-day intervals from day 3 to day 15. The overall response is very similar to that observed with an upper-level cyclonic anomaly forming off the central Western Australian coast by day 3 (Fig. 3a, c.f. Fig. 2a) and a lower-level anticyclonic anomaly over southeast Australia by day 6 (Fig. 3b, c.f. Fig. 2b). A tropical-extratropical wave train clearly emanates away from the Indo-Pacific source of tropical heating towards the southeast as the model simulation progresses. Impressively, the broad structure of the negative–positive–negative geopotential height anomaly response over the high latitudes of the Southern Ocean and South

America from day 9 also resembles that observed, with cyclonic centres seen near 170°W, 60°S and 40°W, 50°S, and an anticyclonic centre near 110°W, 60°S. This result supports the proposed role of the MJO for driving Australian springtime anomalies in circulation and surface climate via its influence on tropical-extratropical wave activity (e.g., Wheeler et al. 2009, Cowan et al. 2022, Marshall et al. 2022b). The simple linear model used here will be the subject of future work for further exploring global teleconnection pathways to the MJO (e.g., Lin et al. 2019).

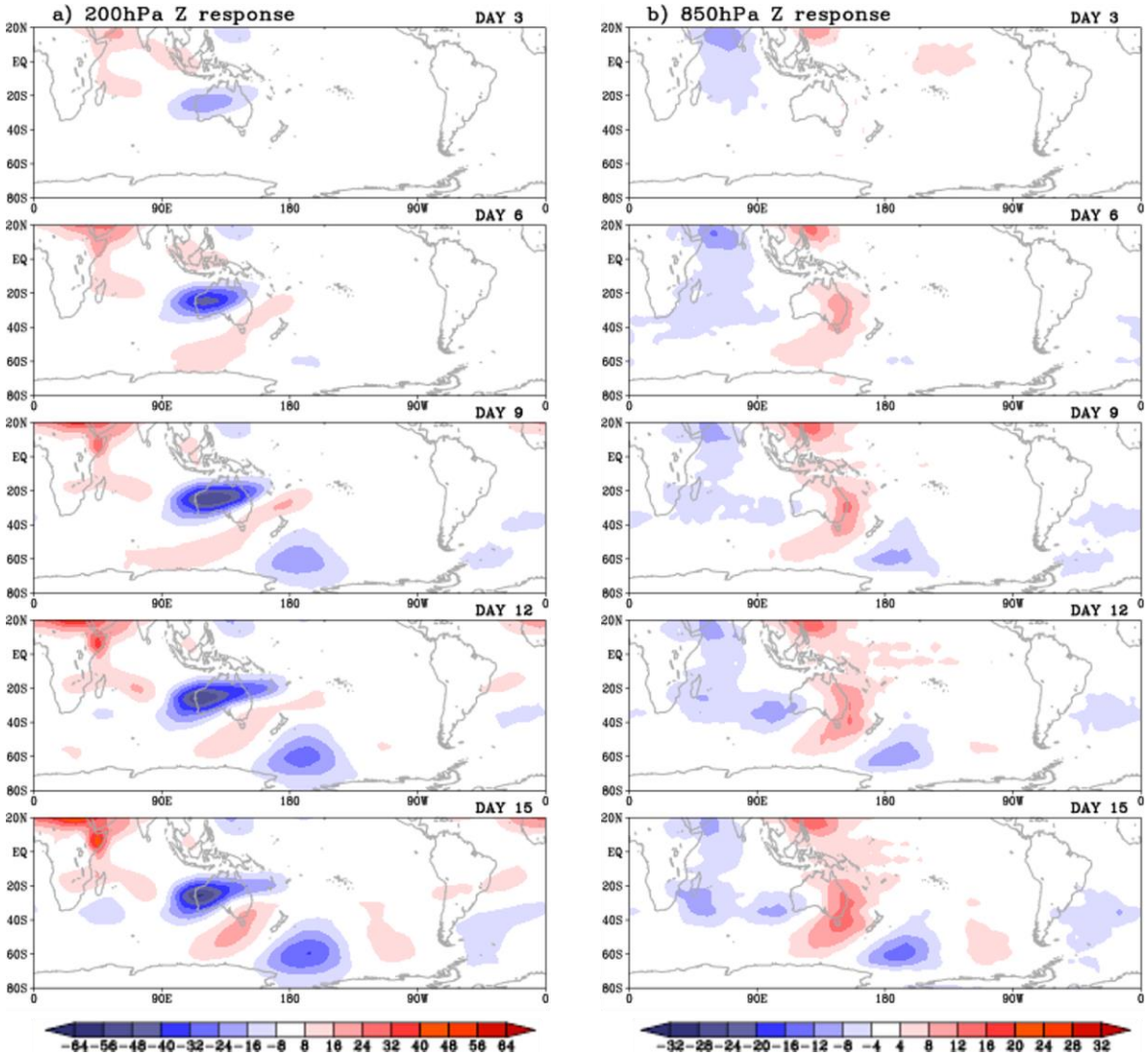

Fig. 3 Simple linear model response to MJO phase 2 in SON for geopotential height anomalies (m) at (a) 200 hPa and (b) 850 hPa, at three-day intervals from day 3 (top) to day 15 (bottom).

4 MJO teleconnection mechanism

a) Rossby Wave Propagation

In the previous section we identified local influences on the strong warming across southern Australia during spring in MJO phases 2 and 3, associated with an anticyclone (high pressure) anomaly over the Tasman Sea (Wheeler et al. 2009, Cowan et al. 2022). The inference here is that the enhanced MJO convection (i.e., diabatic heating) over the Indian Ocean during these phases drives a Rossby wave train response that, in turn, modifies the extratropical circulation and incites warm (and dry) conditions over southern Australia. We quantify this Rossby wave teleconnection pathway here, and demonstrate its evolution through MJO phases 1-4, by presenting WAF and RWS calculations (described in Section 2a) along with 200 hPa streamfunction anomalies and tropical OLR anomalies in Fig. 4.

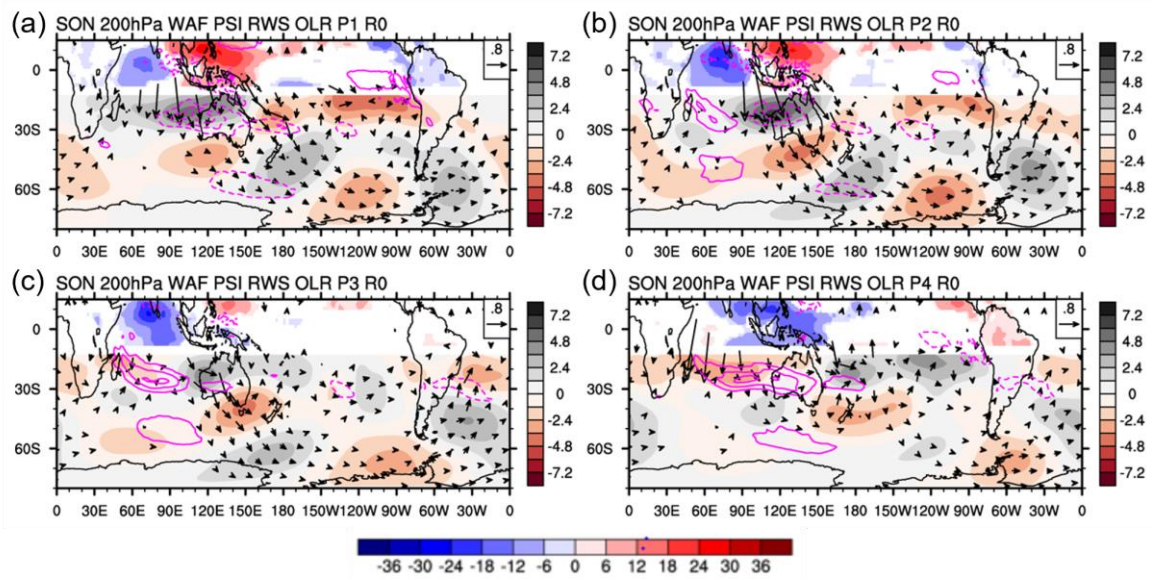

429

430 **Fig. 4** Regressions for MJO phases 1 to 4 (a-d) of 200 hPa wave activity flux (WAF, vector,
431 unit m^2 s^{-2}, scale shown in top-right; weaker vectors omitted for clarity), 200 hPa
432 streamfunction anomaly (shaded field south of 10ºS, interval $1.2x10^6$ m^2s^{-1}, bar on right hand
433 side), OLR anomaly (shaded field north of 10ºS, interval 6 W m^{-2}, bar at bottom), and Rossby
434 wave source advection term S1 (contoured, negative values dashed, zero contour omitted,
435 interval $1.5x10^{-11}$ m^2s^{-1}). In the Southern Hemisphere, positive Rossby wave source means
436 anticyclonic tendency; an anticyclonic anomaly corresponds to negative streamfunction
437 anomaly. Corresponding figures for MJO phase 5 to 8 are identically opposite in sign.

438

439 Concentrating first on the relationship of the streamfunction anomalies
440 (shaded field south of 10 °S) to the MJO's tropical convection anomalies, we see that
441 the anomalous cyclone (grey shaded streamfunction anomaly) centred on the Western
442 Australian coast during phase 1 (Fig. 4a) and phase 2 (Fig. 4b) is shifted by about 30
443 degrees longitude to the west of the suppressed tropical convection (red shaded OLR
444 anomaly). This phasing is typical for upper-level circulation anomalies that trail MJO
445 convective anomalies (e.g., Hendon and Salby 1994). As the MJO continues its
446 eastward propagation into phase 3, the cyclonic anomaly weakens over Australia (in

concert with weaker suppression of convection) and rapidly extends eastward across the Pacific Ocean to South America (e.g., Hendon and Salby 1994; Adames and Wallace 2014). The following surge of enhanced convection (blue shading) intensifies over the eastern Indian Ocean in phase 3 (Fig. 4c), and then moves over the Maritime Continent in phase 4 (Fig. 4d), as an upper-level anticyclone appears to its southwest over South Africa and the southern Indian Ocean.

The cyclonic anomaly over Australia in phases 1-3 is part of a tropical-extratropical wave train that develops in phase 1, matures in phase 2, and continues into phase 3 before dissipating in phase 4. (The wave train is only efficiently forced or permitted during phases 1-3; see also Section 4b.) The WAF vectors confirm the poleward and eastward dispersion of the wave activity along a great circle route from the cyclonic centre over Western Australia towards South America, most pronounced in phase 2. This wave train is very well defined and exhibits an equatorward arc at around 110 °W over the Southern Ocean, along the eddy-driven jet wave guide, towards the south-western Atlantic Ocean (e.g., Alvarez et al. 2016). The anomalous S1 RWS (pink contouring in Fig. 4) confirms a cyclonic tendency (dashed) directly south of the suppressed MJO convection, and an anticyclonic tendency (solid) directly south of the enhanced MJO convection, along the axis of the subtropical jet (25°–30°S). The resulting cyclonic/anticyclonic anomalies appear centred on the western flank of the cyclonic/anticyclonic S1 RWS due to Sverdrup balance; the balance between the RWS vorticity tendency and the meridional rotational flow that advects planetary vorticity poleward (e.g., Hoskins and Karoly 1981; Qin and Robinson 1993; Wang and Hendon 2020).

We also note the wave train that appears over the eastern Pacific Ocean in association with the MJO's modulation of tropical cyclones there (e.g., Maloney and

Hartmann 2001). These MJO-driven convection anomalies drive an anticyclonic source (related to enhanced convection over tropical south America) mostly in phase 1, and a cyclonic source (related to suppressed convection) mostly in phase 4, thus also acting as a S1 RWS for wave activity into the Southern Hemisphere. This appears to contribute to the South American (downstream) component of the wave train that emanates out of the Indian Ocean.

An important aspect of the Indian Ocean Rossby wave teleconnection pathway is its largely stationary characteristic, with little indication of west-east translation through phases 1-3, before its dissipation in phase 4. This characteristic is likely to benefit a dynamical model forecast as the MJO traverses the Indian Ocean, despite any inaccuracies in the MJO's simulated propagation speed. This stationarity is confirmed by computing the root mean square (RMS) amplitude of the MJO 200 hPa streamfunction anomalies over all 8 phases (Fig. 5b). The wave train emanating from the Indian Ocean survives this RMS calculation over all 8 MJO phases, indicating that it re-emerges with opposite sign during MJO phases 5, 6 and 7. The wave train near South America is also somewhat evident in Fig. 5b. These fixed-in-space teleconnections appear partly due to the tropical RWS being fixed in longitude, despite the continuous eastward propagation of the MJO convective anomalies, as is indicated by the RMS of the divergent meridional wind (Fig. 5a). Two localised regions of maximum divergent meridional wind RMS are apparent: a strong one spanning the Indian Ocean – Maritime Continent sector (around 1 m s^{-1}), and a weaker one over the far eastern Pacific (around 0.6 m s^{-1}). For the former, several maxima in divergent meridional wind appear across the tropical Indian Ocean, reflecting the behaviour of MJO convection during austral spring. Specifically, MJO convection anomalies in spring share similarities to those occurring in winter and in

summer, with nodes that straddle the equator over the western Indian Ocean where the convective anomaly develops, and over the Maritime Continent where the convective anomaly intensifies (e.g., Wheeler and Hendon 2004, Wheeler et al. 2009).

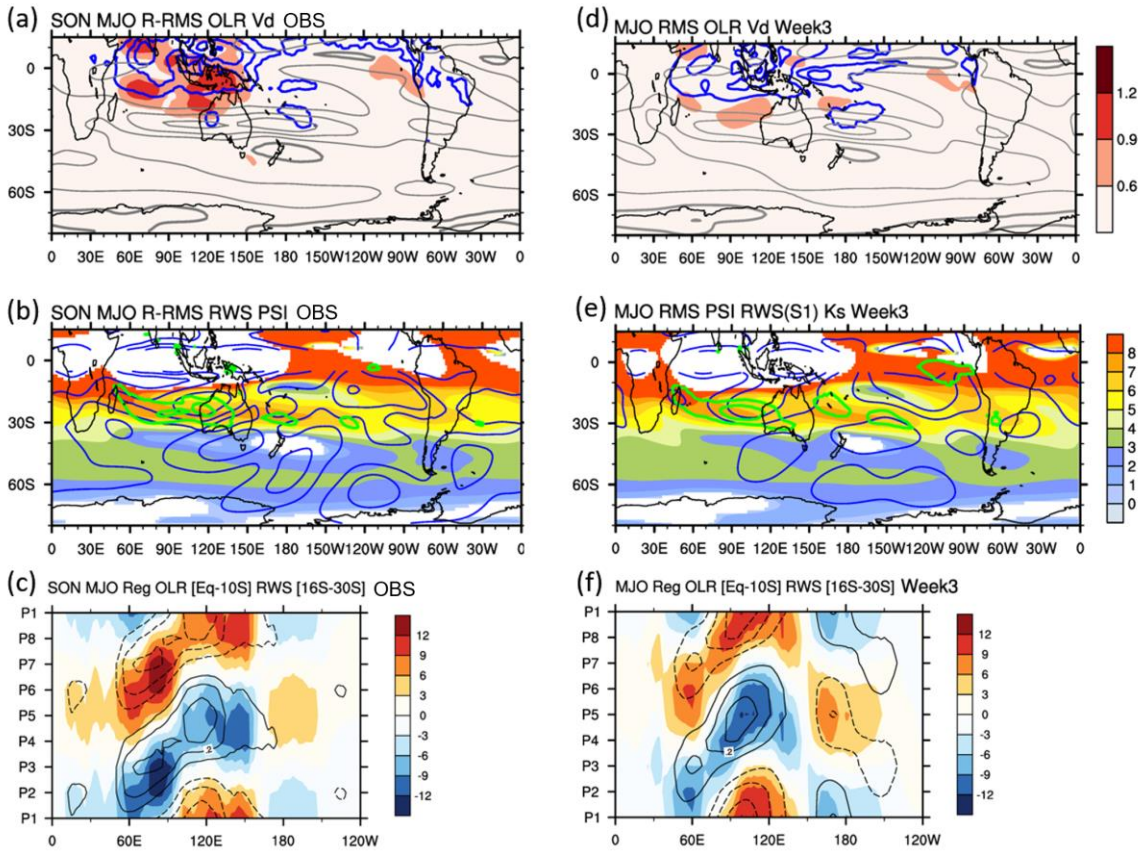

Fig. 5 Observed RMS amplitude of MJO anomalies computed over all 8 phases for (a) OLR (blue contours, interval 5 Wm^{-2}) and meridional component divergent wind at 200 hPa (shading, bar on far right, unit ms^{-1}). The meridional gradient of mean absolute vorticity, β^*, at 200 hPa during SON is contoured (zero is bold thick, interval $2x10^{-11}$ s^{-1} m^{-1}); (b) RWS (fluorescent green contours) and 200 hPa streamfunction (blue contours, interval $1x10^6$ m^2s^{-1}) with the stationary Rossby wave number, K_s (shading, bar on far right), white is indicative of where K_s is undefined, and (c) Longitude vs MJO phase Hovmöller diagram of OLR averaged 0^o to 10^oS (shading, unit W m^{-2}, bar on right) and RWS S1 averaged 16^o to 30^oS (contoured, negative values dashed, zero contour omitted, interval $1x10^{-11}$ m^2 s^{-1}). (d) – (f), same as (a) –

(c) but calculated from ACCESS-S1 forecasts at a lead time of three weeks. Note the longitude ranges in (c) and (f) are aligned with that displayed in the maps above.

Wang and Hendon (2020) showed a similar wave train teleconnection in the Australian sector during austral winter associated with MJO convective anomalies to the north of Australia. They described the role of these MJO anomalies for producing strong S1 RWS, and the dependence of the resulting wave train on the refractive characteristics of the mean state zonal winds. We find a similar result here for the springtime MJO except, unlike that in winter, the wave train in spring can propagate continuously from the Indian Ocean / Australian sector along a great circle path. To summarise these refractive characteristics (see Wang and Hendon 2020 for more detailed discussion), the divergent outflow from anomalous MJO convection acts to advect the mean state absolute vorticity gradient that maximizes along the subtropical jet (Fig. 5a; grey contours). We note that here we distinctly see the wave train as separate from the tropically trapped baroclinic MJO convection. The resultant Rossby wave source is strong over the Australian sector, and comparatively weak over the South American sector, due to differences in the strength of the mean state absolute vorticity gradient, β^*, over these regions. The subtropical jet also acts to localize the region where Rossby wave trains can propagate, due to the extent of refractivity allowed by the mean state zonal winds $\bar{U}$ for the propagation of stationary Rossby waves (Hoskins and Ambrizzi 1993), as described by the stationary Rossby wave number, K_s (= $(\beta^*/\bar{U})^{1/2}$; Hoskins and Karoly 1981). That is, the strong subtropical jet results in negative meridional gradient of absolute vorticity on its poleward flank to the southeast of Australia over New Zealand (Fig. 5a), thus prohibiting tropical-extratropical Rossby wave propagation in this 'no-go zone' where K_s is undefined

(Fig. 5b; white shading). Thus, the MJO is only able to excite Rossby wave trains that disperse across the extratropical Southern Hemisphere when the MJO convection is to the north and west of Australia. (Note that the wave activity directly south of Australia occurs in a region where the absolute vorticity gradient is weakly positive, to the west of the no-go zone; see also McIntosh and Hendon 2018). The relationship between S1 RWS and MJO convection here is further demonstrated in the phase-longitude plot of Fig. 5c, where maxima in anomalous OLR (averaged equatorward of 10 °S) near 60°E, 90°E, and 120-150°E occur in conjunction with strong S1 RWS anomalies (averaged between 16°S and 30°S) in the vicinity of the subtropical jet. This also confirms a cyclonic tendency (dashed RWS contours) associated with suppressed MJO convection (increased OLR; red shading) and an anticyclonic tendency (solid contours) associated with enhanced MJO convection (reduced OLR; blue shading).

b) Role of mid-latitude eddies

Wang and Hendon (2020) detailed for the austral winter MJO case an additional Rossby wave source that likely exists from reorganization of the midlatitude storm track, due to the transient eddies feeding back onto the low frequency flow. We illustrate a similar feedback during spring in Fig. 6, using the eddy-induced streamfunction tendency associated with horizontal convergence of transient eddy vorticity flux at 200 hPa (e.g., Li et al. 2012, Wang and Hendon 2020):

$$\frac{\partial \Psi_{200}}{\partial t} = \nabla^{-2}\left[-\nabla \cdot \overline{\boldsymbol{V}'\zeta'}\right]$$

Primes refer to 7-day cutoff high pass filtered daily anomalies, and the overbar refers to a 7-day low pass mean. The 7-day cut off period enables us to separate the synoptic eddies from the MJO anomalies; see Wang and Hendon 2020 for more details. Displayed here for MJO phases 1-4, we see prominent maxima to the south of Australia and to the east of Argentina in the southwest Atlantic. In MJO phases 1 and 2, these peaks appear as a negative/anticyclonic streamfunction tendency in the Australian sector and a positive/cyclonic streamfunction in the South American sector, aligned with the corresponding anticyclonic and cyclonic anomalies seen in Fig. 4. We note that the peak magnitudes of these feedback terms are around 6 x 10^7 m^{-2} s^{-1} day^{-1}, suggesting that this tendency acting for about 6 days (the typical timespan of an MJO phase; Wheeler and Hendon 2004) could produce the observed streamfunction anomalies in both the Australian and South American sectors (with peak magnitudes of around 3.6 x 10^6 m^{-2} s^{-1}).

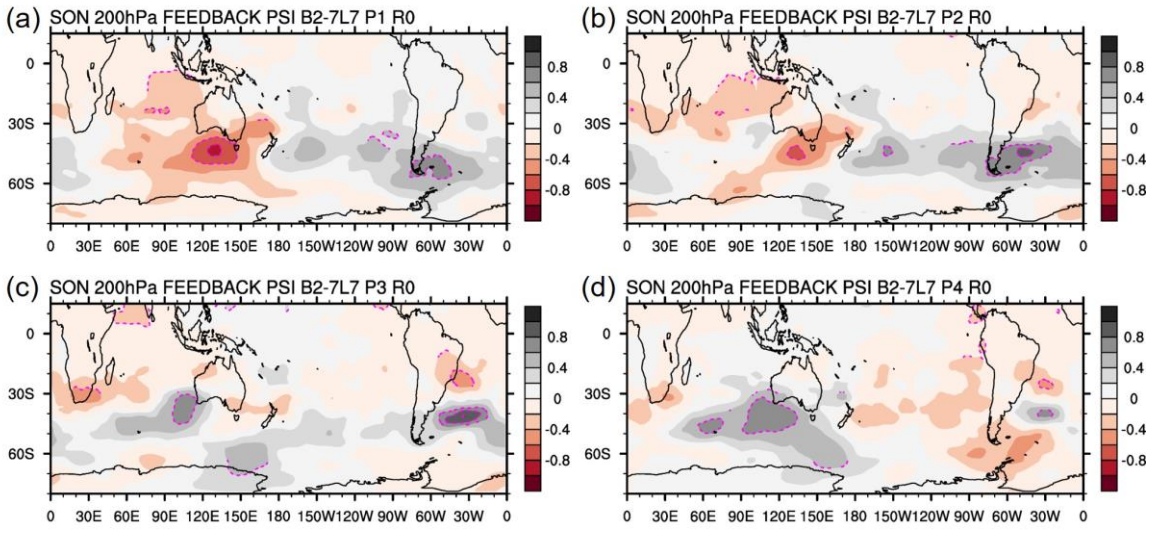

Fig. 6 As in Fig. 4 except for the streamfunction tendency at 200 hPa produced by the barotropic feedback from the high frequency (periods 2 - 7 days) transient eddies. Interval

578 $0.2x10^6$ m^2 s^{-1} day^{-1} (bar on right; negative value is anticyclonic tendency). Dashed contours
579 enclose significant tendencies at $p < 0.05$.

580

581 This barotropic feedback of the transient eddies thus can contribute to (i) the
582 poleward propagating component of the wave train from the anticyclonic peak south
583 of Australia, and (ii) the equatorward propagating component from cyclonic peak near
584 the tip of South America (Fig. 4). The additional RWS in the Australian sector also
585 occurs to the west of the no-go zone, where the meridional gradient of absolute
586 vorticity is weakly positive, although its occurrence on the poleward flank of the no-
587 go zone means that it would likely circumvent the blocking character of the
588 subtropical jet if the no-go zone were to extend directly south of Australia in early
589 spring, as it does through winter (McIntosh and Hendon 2018, Wang and Hendon
590 2020)

591 As the MJO continues its eastward propagation into phase 3, the anticyclonic
592 tendency weakens and distorts to the southeast of Australia (again in concert with
593 weaker suppression of convection) as a positive/cyclonic streamfunction tendency
594 develops off the southwest Australian coast. The demise of the Rossby wave train in
595 phase 4 (Fig. 4) is likely influenced by the eastward extension of this cyclonic
596 tendency directly to the south of Australia (Fig. 6), which would act against the
597 anticyclonic anomalies that had prevailed in phases 1-3 and thereby disrupt the
598 feedback.

599

600 **5 Prediction in ACCESS-S1**

601

We assess the ability of ACCESS-S1 to predict the MJO's impacts on Australian springtime temperatures, and the associated Rossby wave teleconnection into the Southern Hemisphere, at lead times of two, three and four weeks. Regression calculations for ACCESS-S1 are carried out using the ensemble mean, rather than individual ensemble members, to consider model performance from the perspective of operational deterministic forecasting (e.g., Gottschalck et al. 2010; Hudson et al. 2017). Forecast regressions of maximum temperature during MJO phase 2 in Figs. 7b-d show broad agreement with the observed regressions (reproduced in Fig. 7a) at each lead time, except the warm signal appears shifted too far west, most noticeably in week 2 of the forecast. Compared to observations (reproduced in Fig. 7e), the forecast Rossby wave activity in the Australian region during phase 2 is also shifted further to the west, by about 10-20 ° of longitude, at all lead times (Figs. 7f-h). These signals also weaken with lead time, particularly the 200 hPa streamfunction (cyclonic) anomaly and corresponding surface maximum temperature anomaly near the central Western Australian coast. Regardless, ACCESS-S1 captures well the phasing between MJO convection and upper-level circulation anomalies in the Australian region (e.g., Hendon and Salby 1994).

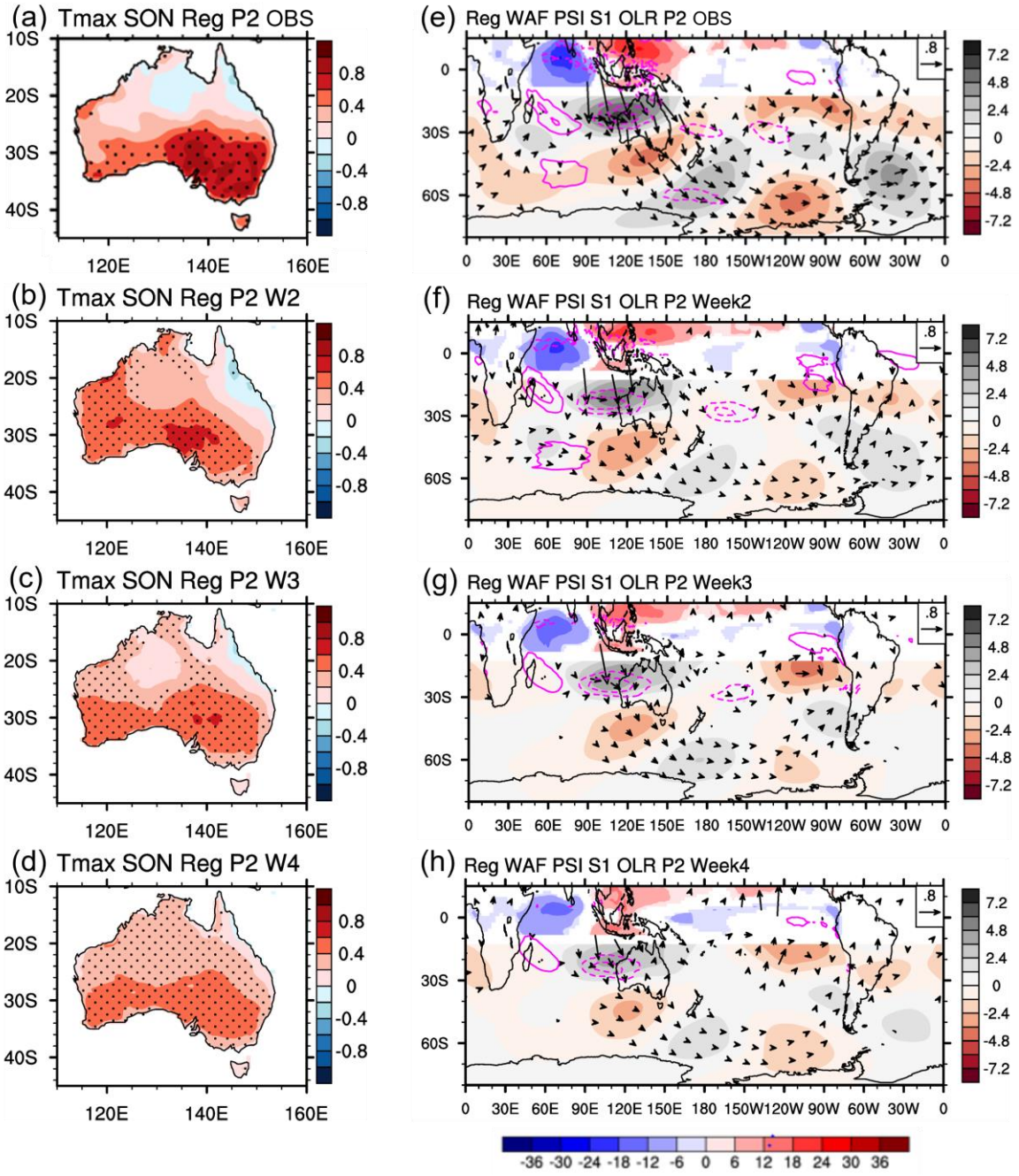

Fig. 7 Forecast regressions for MJO phase 2 and at lead week 2 of (b) maximum temperature anomaly, and (f) 200 hPa wave activity flux (WAF, vector, unit $m^2\ s^{-2}$, scale shown in top-right; weaker vectors omitted for clarity), 200 hPa streamfunction anomaly (shaded field south of 10ºS, interval $1.2x10^6\ m^2\ s^{-1}$, bar on right hand side), OLR anomaly (shade field north of 10ºS, interval 6 W m^{-2}, bar at bottom), and RWS S1 (contoured, negative values dashed, zero contour omitted, interval $1.5x10^{-11}\ m^2\ s^{-1}$). (c), (g) same as (b), (f) but for lead week 3; (d), (h) same as (b), (f) but for lead week 4. (a) and (e) are observed regressions for

MJO phase 2 reproduced from Figs. 1a and 4b respectively, for ease of comparison. The regression coefficients are scaled for a normalized MJO amplitude of 1.5.

The poleward and eastward dispersion of the wave activity along a great circle route from the cyclonic centre over Western Australia towards South America is broadly well defined in ACCESS-S1, as is the wave train that appears over the eastern Pacific Ocean in association with the MJO's modulation of tropical cyclones there (e.g., Maloney and Hartmann 2001). However, as the teleconnection signal weakens over Australia into weeks three and four, so too does its downstream component over the southwest Atlantic Ocean. At the same time its equatorward arc shifts closer to 130 °W – about 20 ° to the west of that observed – resulting in a deterioration of wave activity flux over the southwest Atlantic. Consequently, the Rossby wave pathway reorganises over South America instead.

The weaker than observed teleconnection in ACCESS-S1 is further demonstrated for week three of the forecast in Fig. 5 (d-f). While the forecast RMS calculations capture the fixed-in-space characteristic of the Indian Ocean Rossby wave teleconnection pathway, both the 200 hPa streamfunction anomaly (Fig. 5d) and divergent meridional wind (Fig. 5e) RMS signals are around half the strength of those observed over the Indian Ocean – Maritime Continent sector. Importantly, this occurs in conjunction with a weaker than observed negative OLR anomaly over the Indian Ocean (between about 60 °E and 90°E), and a westward-shifted maximum in anomalous OLR over the Maritime Continent (centred around 105 °E in ACCESS-S1, compared to around 135 °E in observations) (Fig. 5f). In Table 1 we show the forecast MJO variability to decrease with lead time, with RMM bivariate index standard deviation values falling from 0.82 in week 1 to 0.57 in week 4, compared to an

observed value of 0.93. These biases in the model's depiction of the MJO are thus likely to affect the strength and location of (i) the divergent outflow from the tropics (Fig. 5d; shading) onto the mean state absolute vorticity gradient, which also appears weaker than that observed (Fig. 5d; grey contours) and (ii) the resultant Rossby wave source over the Australian sector (Fig. 5e; fluorescent green contours and Fig. 5f; black contours). The downstream impact of this can be seen in the weakening and westward displacement of the model's 200 hPa streamfunction anomaly RMS (Fig. 5e; blue contours), compared to that observed (Fig. 5b; blue contours). The model's 'no-go zone' for Rossby waves near the subtropical jet (Fig. 5e; white shading) is smaller than that observed, occurring only to the east of New Zealand. While this permits the great circle teleconnection pathway in the Australian sector, it implies errors in the model's depiction of the subtropical jet which will also influence the simulation and prediction of MJO-induced climate anomalies across southern Australia.

Table 1: RMM bivariate index standard deviation (centre column) and forecast correlation skill (right column; following Lin et al. 2008) using ACCESS-S1 ensemble mean forecasts initialised in September, October, and November at lead times of one to four weeks. Also shown is the observed RMM bivariate index standard deviation for comparison (bottom row).

Dataset	Standard Deviation	Correlation
Week 1	0.82	0.86
Week 2	0.70	0.76
Week 3	0.62	0.70
Week 4	0.57	0.55

Observations	**0.93**	

Finally, we explore the ability of ACCESS-S1 to predict maximum temperature anomalies in both the top and bottom quintiles over Australia at lead times of two, three and four weeks, in association with the MJO during spring. For this we calculate the forecast success ratio (SR) when the MJO is active at the initial time (Fig. 8a), when the MJO is inactive at the initial time (Fig. 8b), and for the active-minus-inactive MJO difference (Fig. 8c). The SR is the proportion of forecast hits calculated relative to the total number of forecast top and bottom quintile events, and thus measures the fraction of forecast events that were correctly observed:

$$SR = \frac{hits}{hits + false\ alarms}$$

Here, *hits* are when top and bottom quintile events were forecast to occur and did occur, and *false alarms* are when top and bottom quintile events were forecast to occur but did not occur. The forecast SR is seen to deteriorate with lead time, consistent with decreasing forecast MJO variability and MJO bivariate correlation skill (Table 1). Impressively, at each lead time a higher SR for predicting top and bottom quintile events is achieved over large parts of Australia when the MJO is active at the initial time, compared to when the MJO is inactive. Importantly, improvements in forecast SR occur over much of southern Australia at all lead times, particularly in the southeast where the MJO has its largest impact on maximum temperature during spring. Thus, the MJO is a source of subseasonal predictability for

springtime heat and cold events over southern Australia that are remotely driven by its convective anomalies over the Indian Ocean in phases 1-3 (heat events; Fig. 1) and oppositely in phases 5-7 (cold events; not shown).

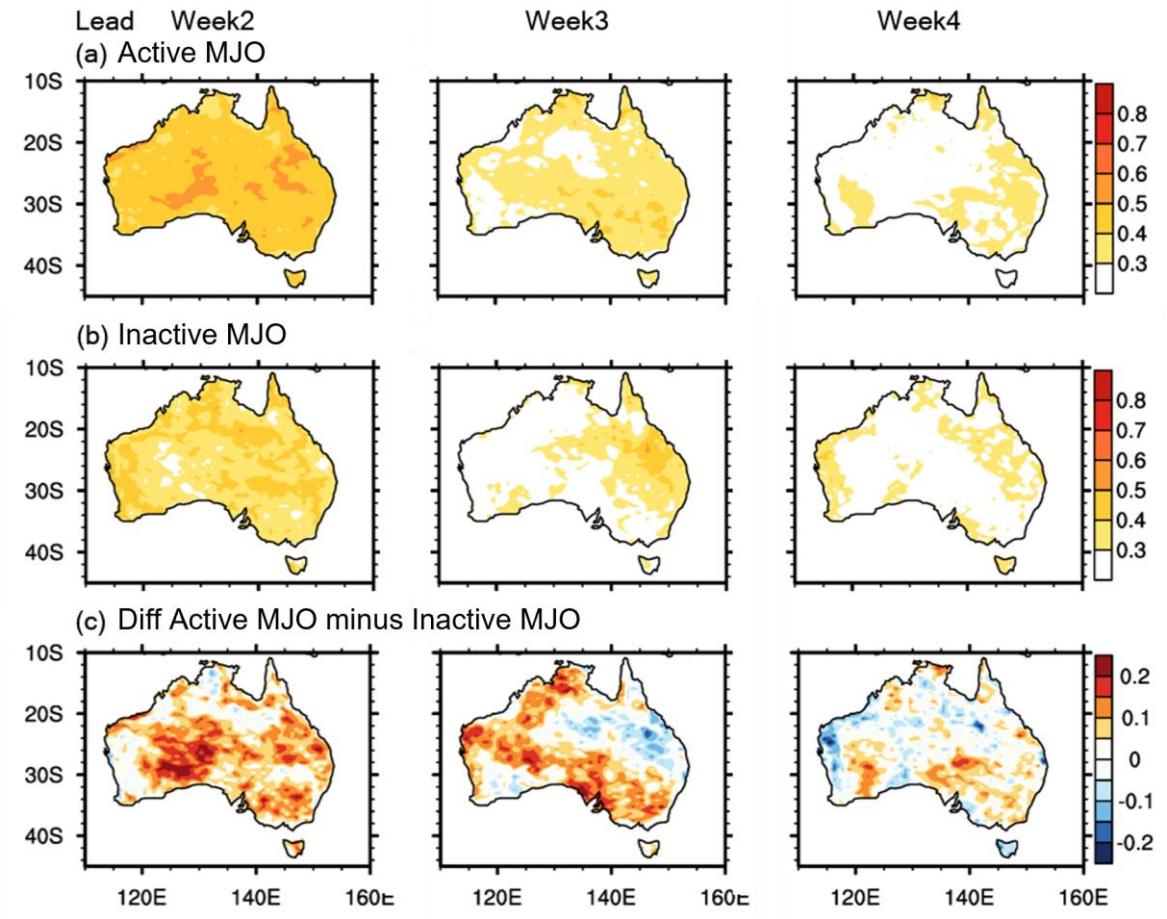

Fig. 8 Success ratio (SR) metric over Australia for springtime maximum temperature in both top and bottom quintiles at lead week 2 to 4 when (a) MJO is active, and (b) MJO is inactive. (c) SR difference between active and inactive MJOs.

6 Summary and conclusions

We have shown the MJO to modulate springtime temperatures across much of southern Australia, particularly the southeast, where strong and significant increases

occur in MJO phases 2, 3 and 4 for maximum and minimum temperature, including an increased likelihood of extreme (top quintile) daytime heat. This warming is associated with a strong and deep anticyclonic anomaly that centres over southeast Australia and the Tasman Sea and extends across the continent, bringing anomalously warm easterly and north-easterly wind flow to the southwest while promoting shortwave radiative heating in the southeast. The heat signal is strongest in phases 2 and 3 when MJO convection is enhanced over the Indian Ocean. Our regression analysis produces an equal and opposite cold signal in southern Australia during MJO phases 6 and 7 when MJO convection is suppressed over the Indian Ocean, however we focus mostly on the springtime heat signal in this study due to its known importance for human health, agriculture, and fire management (e.g., Marshall et al. 2022a).

This local signal over Australia occurs as part of a planetary scale circulation response to the MJO in the form of stationary tropical-extratropical Rossby wave trains. These MJO-forced wave trains develop in phase 1, mature in phase 2, and continue into phase 3 before dissipating in phase 4. Wave activity fluxes illustrate their poleward and eastward dispersion from the Indian Ocean / Australian sector towards South America, arcing over the Southern Ocean towards the south-western Atlantic Ocean along a great circle route. A second concurrent wave train over the eastern Pacific, associated with MJO-modulated tropical cyclone activity, contributes to the South American component of the wave train that emanates out of the Indian Ocean. These wave trains re-emerge with opposite sign during MJO phases 5, 6, and 7 (i.e., in conjunction with suppressed MJO convection over the Indian Ocean and cold conditions in southern Australia).

Following Wang and Hendon (2020) and McIntosh and Hendon (2018), we show the dispersion characteristics of the wave train over Australia to be determined by (i) the location of divergent outflow from anomalous MJO convection (consistent with Mori and Watanabe 2008 and Frederiksen and Lin 2013), which creates a strong Rossby wave source in the Australian sector, and (ii) the refractive characteristics of the mean state zonal winds, which create a prohibitive 'no-go' zone for Rossby waves on the poleward flank of the subtropical jet to the south and east of Australia where the meridional gradient of absolute vorticity is negative. Thus, the MJO is only able to excite Rossby wave trains that disperse across the extratropical Southern Hemisphere when the MJO convective anomalies are to the north and west of Australia, i.e., over the tropical Indian Ocean. We also identified an additional Rossby wave source that exists from reorganization of the midlatitude storm track, due to the transient eddies feeding back onto the low frequency flow, to the south of Australia and to the southeast of South America. This feedback contributes to the wave train activity in both regions during phases 1, 2 and 3 until its disruption in phase 4, which likely influences the demise of the Rossby wave train at that time (and likewise for the opposite signed wave activity in phases 5-8).

Subseasonal forecasts from the Bureau of Meteorology's subseasonal to seasonal prediction system ACCESS-S, version 1, show broad agreement with the observed impacts of the MJO on Australian springtime temperatures and associated Rossby wave activity at lead times of two, three and four weeks. Some notable model biases emerge, however, including a westward shift in the teleconnection patterns by about 20 ° of longitude, and a general weakening of the signals with increasing lead time. These biases largely stem from errors in the model's representation of MJO convective anomalies over the Indian Ocean (weaker than observed) and Maritime

Continent (shifted westward), which grow with lead time and affect the strength and location of (i) the divergent outflow from the tropics onto the mean state absolute vorticity gradient, and (ii) the resultant Rossby wave source over the Australian sector. This in turn affects the teleconnection downstream, particularly over the southwest Atlantic Ocean where the equatorward wave activity flux deteriorates in weeks three and four of the forecast. Despite these model errors, ACCESS-S1 demonstrates the ability to better predict top and bottom quintile maximum temperature anomalies over southern Australia when the MJO is active at the initial time, compared to when the MJO is inactive at the initial time, particularly in the southeast. The MJO is thus a source of multiweek predictability of springtime heat and cold events where its impact on temperatures and extremes is most prevalent.

The next generation of the ACCESS-S prediction system, version 2, became operational at the Bureau of Meteorology in October 2021. The main changes between ACCESS-S1 and ACCESS-S2 - ocean and land initialisation - have had minimal impact on subseasonal prediction skill for Australian climate and virtually no impact on MJO prediction skill (Wedd et al. 2022). However, future versions will address existing model deficiencies such as rainfall and sea surface temperature biases in the Indian Ocean and Maritime Continent regions, which are known to be important for the MJO and its global teleconnections. We therefore look forward to further improvements in simulating and predicting the MJO Rossby wave teleconnection to Australian climate, including its subseasonal modulation of springtime temperatures and extremes, with subsequent upgrades to the model.

References

782 Adames ÁF, Wallace JM (2014) Three-dimensional structure and evolution of the
783 MJO and its relation to the mean flow. J Atmos Sci 71:2007–2026.
784 https://doi.org/10.1175/JAS-D-13-0254.1
785
786 Alvarez MS, Vera CS, Kiladis GN, Liebmann B (2016) Influence of the Madden
787 Julian Oscillation on precipitation and surface air temperature in South America. Clim
788 Dyn 46:245–262. https:// doi.org/10.1007/s00382-015-2581-6
789
790 Alves O, Wang G, Zhong A, Smith N, Tzeitkin F, Warren G, Schiller A, Godfrey S,
791 Meyers G (2003) POAMA: Bureau of Meteorology Operational Coupled Model
792 Forecast System. In: Proceedings of national drought forum, Brisbane, April 2003, pp
793 49-56. DPI Publications, Department of Primary Industries, Brisbane
794
795 Becker EJ, Berbery EH, Higgins RW (2011) Modulation of Cold-Season U.S. daily
796 precipitation by the Madden–Julian Oscillation. J Clim 24:5157–5166.
797 https://doi.org/10.1175/2011JCLI4018.1
798
799 Bergman JW, Hendon HH, Weickmann KM (2001) Intraseasonal Air–Sea
800 Interactions at the Onset of El Niño. J Clim 14:1702–1719.
801 https://doi.org/10.1175/1520-0442(2001)014<1702:IASIAT>2.0.CO;2
802
803 Bond NA, Vecchi GA (2003) The Influence of the Madden–Julian Oscillation on
804 Precipitation in Oregon and Washington. Weather Forecast 18:600–613.
805 https://doi.org/10.1175/1520-0434(2003)018<0600:TIOTMO>2.0.CO;2
806

807 Bretherton CS, Widmann M, Dymnikov VP, Wallace JM, Bladé I (1999) The
808 effective number of spatial degrees of freedom of a time-varying field. J Clim
809 12:1990–2009. https://doi.org/10.1175/1520-
810 0442(1999)012<1990:TENOSD>2.0.CO;2
811
812 Camargo SJ, Wheeler MC, Sobel AH (2009) Diagnosis of the MJO modulation of
813 tropical cyclogenesis using an empirical index. J Atmos Sci 66:3061–3074.
814 https://doi.org/10.1175/2009jas3101.1
815
816 Camp J, Wheeler MC, Hendon HH, Gregory P, Marshall AG, Tory KJ, Watkins AB,
817 MacLachlan C, Kuleshov Y (2018) Skilful multi-week tropical cyclone prediction in
818 ACCESS-S1 and the role of the MJO. Q J R Meteorol Soc 144:1337–1351.
819 https://doi.org/10.1002/qj.3260
820
821 Cowan T, Wheeler MC, Marshall AG (2022) The combined influence of the Madden-
822 Julian Oscillation and El Niño–Southern Oscillation on Australian rainfall. J Clim,
823 accepted
824
825 Dee DP, Uppala SM, Simmons AJ, Berrisford P, Poli P, Kobayashi S, Andrae U,
826 Balmaseda MA, Balsamo G, Bauer P, Bechtold P, Beljaars ACM, van de Berg L,
827 Bidlot J, Bormann N, Delsol C, Dragani R, Fuentes M, Geer AJ, Haimberger L, Healy
828 SB, Hersbach H, Hólm EV, Isaksen L, Kållberg P, Köhler M, Matricardi M, McNally
829 AP, Monge-Sanz BM, Morcrette J-J, Park B-K, Peubey C, de Rosnay P, Tavolato C,
830 Thépaut J-N, Vitart F (2011) The ERA-Interim reanalysis: configuration and

831 performance of the data assimilation system. Q J R Meteorol Soc 137:553–597.
832 https://doi.org/10.1002/ qj.828
833
834 Frederiksen JS, Lin H (2013) Tropical-Extratropical Interactions of Intraseasonal
835 Oscillations. J Atmos Sci 70:3180–3197. doi:10.1175/JAS-D-12-0302.1
836
837 Gill AE (1980) Some simple solutions for heat-induced tropical circulation. Q J R
838 Meteorol Soc 106:447–462. https://doi.org/10.1002/qj.49710644905
839
840 Gottschalck J, Wheeler M, Weickmann K, Vitart F, Savage N, Lin H, Hendon H,
841 Waliser D, Sperber K, Nakagawa M, Prestrelo C, Flatau M, Higgins W (2010) A
842 Framework for Assessing Operational Madden–Julian Oscillation Forecasts. Bull Am
843 Meteorol Soc 91:1247–1258. https://doi.org/10.1175/2010BAMS2816.1
844
845 Grimm AM (2019) Madden-Julian Oscillation impacts on South American summer
846 monsoon season: precipitation anomalies, extreme events, teleconnections, and role in
847 the MJO cycle. Clim Dyn 53:907–932. https://doi.org/10.1007/s00382-019-04622-6
848
849 Hall NMJ (2000) A simple GCM based on dry dynamics and constant forcing. J
850 Atmos Sci 57:1557–1572. https://doi.org/10.1175/1520-
851 0469(2000)057<1557:ASGBOD>2.0.CO;2
852
853 Hall NMJ, Derome J (2000) Transients, nonlinearity, and eddy feedback in the remote
854 response to El Niño. J Atmos Sci 57:3992–4007. https://doi.org/10.1175/1520-
855 0469(2001)058<3992:TNAEFI>2.0.CO;2

Hendon HH, Liebmann B (1990) The intraseasonal (30–50 day) oscillation of the Australian summer monsoon. J Atmos Sci 47:2909–2924. https://doi.org/10.1175/1520-0469(1990)047<2909:TIDOOT>2.0.CO;2

Hendon HH, Salby ML (1994) The life cycle of the Madden–Julian Oscillation. J Atmos Sci 51:2225–2237. https://doi.org/10.1175/1520-0469(1994)051<2225:TLCOTM>2.0.CO;2

Hendon HH, Thompson DWJ, Wheeler MC (2007) Australian Rainfall and Surface Temperature Variations Associated with the Southern Hemisphere Annular Mode. J Clim 20:2452-2467. https://doi.org/10.1175/JCLI4134.1

Hoskins BJ, Ambrizzi T (1993) Rossby wave propagation on a realistic longitudinally varying flow. J Atmos Sci 50:1661–1671. https://doi.org/10.1175/1520-0469(1993)0502.0.CO;2

Hoskins BJ, Karoly DJ (1981) The steady linear response of a spherical atmosphere to thermal and orographic forcing. J Atmos Sci 38:1179–1196. https://doi.org/10.1175/1520- 0469(1981)0382.0.CO;2

Hudson D, Alves O, Hendon HH, Lim E-P, Liu G, Luo JJ, MacLachlan C, Marshall AG, Shi L, Wang G, Wedd R, Young G, Zhao M, Zhou X (2017) ACCESS-S1: The new Bureau of Meteorology multi-week to seasonal prediction system. J South Hem Earth Sys Sci 67:132–159. https://doi.org/10.1071/ES17009

Janicot S, Caniaux G, Chauvin F, de Coëtlogon G, Fontaine B, Hall N, Kiladis G, Lafore J-P, Lavaysse C, Lavender SL, Leroux S, Marteau R, Mounier F, Philippon N, Roehrig R, Sultan B, Taylor CM (2011) Intraseasonal variability of the West African monsoon. Atmos Sci Lett 12:58–66. https://doi.org/10.1002/asl.280

Jones DA, Wang W, Fawcett R (2009) High-quality spatial climate data-sets for Australia. Aust Meteorol Oceanogr J 58:233–248. https://doi.org/10.22499/2.5804.003

Kessler WS, Kleeman R (2000) Rectification of the Madden-Julian Oscillation into the ENSO Cycle. J Clim 13:3560–3575

Klotzbach PJ (2014) The Madden–Julian oscillation's impacts on worldwide tropical cyclone activity. J Clim 27:2317–2330. https://doi.org/10.1175/jcli-d-13-00483.1

Lau WKM, Waliser DE, Goswami BN (2012) South Asian monsoon. In: Intraseasonal variability in the atmosphere-ocean climate system. Springer Praxis Books, Springer, Berlin, pp 21–72. https://doi.org/10.1007/978-3-642-13914-7_2

Leroy A, Wheeler MC (2008) Statistical prediction of weekly tropical cyclone activity in the Southern Hemisphere. Mon Weather Rev 136:3637–3654. https://doi.org/10.1175/2008mwr2426.1

905 Liebmann B, Hendon HH, Glick JD (1994) The relationship between tropical
906 cyclones of the western Pacific and Indian Oceans and the Madden–Julian oscillation.
907 J Meteorol Soc Japan 72:401–412. https://doi.org/10.2151/jmsj1965.72.3_401
908
909 Liebmann B, Smith CA (1996) Description of a complete (interpolated) outgoing
910 longwave radiation dataset. Bull Am Meteorol Soc 77:1275–1277
911
912 Li Y, Lau N-C (2012) Impact of ENSO on the atmospheric variability over the North
913 Atlantic in late Winter—role of transient eddies. J Clim 25:320–342.
914 https://doi.org/10.1175/JCLI-D-11-00037.1
915
916 Lin H, Brunet G, Derome J (2008) Forecast skill of the Madden–Julian Oscillation in
917 two Canadian atmospheric models. Mon Weather Rev 136:4130–4149.
918 https://doi.org/10.1175/2008MWR2459.1
919
920 Lin H, Brunet G (2009) The influence of the Madden–Julian Oscillation on Canadian
921 wintertime surface air temperature. Mon Weather Rev 137:2250–2262.
922 https://doi.org/10.1175/2009MWR2831.1
923
924 Lin H, Brunet G, Mo R (2010) Impact of the Madden–Julian oscillation on wintertime
925 precipitation in Canada. Mon Weather Rev 138:3822–3839.
926 https://doi.org/10.1175/2010MWR3363.1
927
928 Lin H, Frederiksen J, Straus DM, Stan C (2019) Tropical-Extratropical interactions
929 and teleconnections. In: Robertson AW, Vitart F (eds) Sub-seasonal to

930 seasonal prediction: The gap between weather and climate forecasting. Elsevier,
931 Amsterdam, pp 143–164. https://doi.org/10.1016/B978-0-12-811714-9.00007-3
932
933 Lin H (2022) The Madden-Julian Oscillation. Atmos-Ocean 60:338–359.
934 https://doi.org/10.1080/07055900.2022.2072267
935
936 Lyu M, Jiang X, Wu Z (2019) A cautionary note on the long-term trend in activity of
937 the Madden-Julian Oscillation during the past decades. Geophys Res Lett 46:14063–
938 14071. https://doi.org/10.1029/2019GL086133
939
940 MacLachlan C, Arribas A, Peterson KA, Maidens A, Fereday D, Scaife AA, Gordon
941 M, Vellinga M, Williams A, Comer RE, Camp J, Xavier P, Madec G (2015) Global
942 seasonal forecast system version 5 (GloSea5): a high-resolution seasonal forecast
943 system. Q J R Meteorol Soc 141:1072–1084. https://doi.org/10.1002/qj.2396
944
945 Madden RA, Julian PR (1971) Detection of a 40–50 day oscillation in the zonal wind
946 in the tropical Pacific. J Atmos Sci 28:702–708. https://doi.org/10.1175/1520-
947 0469(1971)028<0702:DOADOI>2.0.CO;2
948
949 Madden RA, Julian PR (1972) Description of global-scale circulation cells in the
950 tropics with a 40–50 day period. J Atmos Sci 29:1109–1123.
951 https://doi.org/10.1175/1520-0469(1972)029<1109:DOGSCC>2.0.CO;2
952
953 Maloney ED, Hartmann DL (2001) The Madden–Julian Oscillation, Barotropic
954 Dynamics, and North Pacific Tropical Cyclone Formation. Part I: Observations. J

955 Atmos Sci 58:2545–2558. https://doi.org/10.1175/1520-
956 0469(2001)058<2545:TMJOBD>2.0.CO;2
957
958 Marshall AG, Alves O, Hendon HH (2009) A coupled GCM analysis of MJO activity
959 at the onset of El Nino. J Atmos Sci 66:966–983.
960 https://doi.org/10.1175/2008JAS2855.1
961
962 Marshall AG, Hudson D, Wheeler MC, Alves O, Hendon HH, Pook MJ, Risbey JS
963 (2014) Intra-seasonal drivers of extreme heat over Australia in observations and
964 POAMA-2. Clim Dyn 43:1915–1937. https://doi.org/10.1007/S00382-013-2016-1
965
966 Marshall AG, Hendon HH (2015) Subseasonal Prediction of Australian Summer
967 Monsoon Anomalies. Geophys Res Lett 42:10913–10919.
968 https://doi.org/10.1002/2015GL067086
969
970 Marshall AG, Hendon HH, Durrant TH, Hemer MA (2015) Madden Julian Oscillation
971 impacts on global ocean surface waves. Ocean Mod, 96:136–147.
972 https://doi.org/10.1016/j.ocemod.2015.06.002
973
974 Marshall AG, Hendon HH, Wang G (2016) On the role of anomalous ocean surface
975 temperatures for promoting the record Madden-Julian Oscillation in March 2015.
976 Geophys Res Lett 43:472–481. https://doi.org/10.1002/2015GL066984
977
978 Marshall AG, Gregory PA, de Burgh-Day CO, Griffiths M (2022a) Subseasonal
979 drivers of extreme fire weather in Australia and its prediction in ACCESS-S1 during

spring and summer. Clim Dyn 58:523–553. https://doi.org/10.1007/s00382-021-05920-8

Marshall AG, Wheeler MC, Cowan T (2022b) Madden-Julian Oscillation impacts on Australian temperatures and extremes. J Clim, accepted

Matthews AJ, Hoskins BJ, Masutani M (2004) The global response to tropical heating in the Madden–Julian oscillation during the northern winter. Q J R Meteorol Soc 130:1991–2011. https://doi.org/10.1256/qj.02.123

McIntosh PC, Hendon HH (2018) Understanding Rossby wave trains forced by the Indian Ocean Dipole. Clim Dyn 50:2783–2798. https://doi.org/10.1007/s00382-017-3771-1

McPhaden MJ (1999) Genesis and evolution of the 1997–98 El Niño. Sci 283:950–954. https://doi.org/10.1126/science.283.5404.950

Mogensen K, Balmaseda MA, Weaver AT, Martin M, Vidard A (2009) Nemovar: A variational data assimilation system for the NEMO ocean model. ECMWF Newsl 120:17–22

Mogensen K, Balmaseda MA, Weaver AT (2012) The NEMOVAR ocean data assimilation system as implemented in the ECMWF ocean analysis for System 4. ECMWF Tech Mem 668:1–59

Mori M, Watanabe M (2008) The growth and triggering mechanisms of the PNA: A MJO-PNA coherence. J Meteorol Soc Japan 86:213–236. https://doi.org/10.2151/jmsj.86.213

Qin J, Robinson WA (1993) On the Rossby wave source and the steady linear response to tropical forcing. J Atmos Sci 50:1819–1823. https://doi.org/10.1175/1520-0469(1993)050<1819:OTRWSA>2.0.CO;2

Ramsay HA, Camargo SJ, Kim D, (2012) Cluster analysis of tropical cyclone tracks in the Southern Hemisphere. Clim Dyn 39:897–917. https://doi.org/10.1007/s00382-011-1225-8

Rashid H, Hendon HH, Wheeler M, Alves O (2011) Prediction of the Madden-Julian Oscillation with the POAMA dynamical seasonal prediction system. Clim Dyn 36:649–661

Reid JS, Xian P, Hyer EJ, Flatau MK, Ramirez EM, Turk FJ, Sampson CR, Zhang C, Fukada EM, Maloney ED (2012) Multi-scale meteorological conceptual analysis of observed active fire hotspot activity and smoke optical depth in the Maritime Continent. Atmos Chem Phys 12:2117–2147. https://doi.org/10.5194/acp-12-2117-2012

Sasikumar K, Nath D, Wang X, Chen W, Yang S (2022) Recent enhancement and prolonged occurrence of MJO over the Indian Ocean and their impact on Indian summer monsoon rainfall. Clim Dyn. https://doi.org/10.1007/s00382-022-06230-3

Stockdale TN (1997) Coupled Ocean–Atmosphere Forecasts in the Presence of Climate Drift. Mon Weather Rev 125:809–818

Straub KH (2013) MJO initiation in the real-time multivariate MJO index. J Clim 26:1130–1151. https://doi.org/10.1175/JCLI-D-12-00074.1

Student (1908) The probable error of a mean. Biometrika 6:1–25. https://doi.org/10.2307/2331554

Takaya K, Nakamura H (2001) A Formulation of a phase-independent wave-activity flux for stationary and migratory quasigeostrophic eddies on a zonally varying basic flow. J Atmos Sci 58:608–627. https://doi.org/10.1175/1520-0469(2001)0582.0.CO;2

Virts KS, Wallace JM (2014) Observations of temperature, wind, cirrus, and trace gases in the tropical tropopause transition layer during the MJO. J Atmos Sci 71:1143–1157. https://doi.org/10.1175/ JAS-D-13-0178.1

Wang G, Hendon HH (2020) Impacts of the Madden–Julian Oscillation on wintertime Australian minimum temperatures and Southern Hemisphere circulation. Clim Dyn 55:3087–3099. https://doi.org/10.1007/s00382-020-05432-x

Wedd R, Alves O, de Burgh-Day C, Down C, Griffiths M, Hendon HH, Hudson D, Li S, Lim E-P, Marshall AG, Shi L, Smith P, Smith G, Spillman CM, Wang G, Wheeler MC, Yan H, Yin Y, Young G, Zhao M, Yi X, Zhou X (2022) ACCESS-S2: The

upgraded Bureau of Meteorology multi-week to seasonal prediction system. J South Hem Earth Sys Sci, submitted

Wheeler MC, Hendon HH (2004) An All-Season Real-Time Multivariate MJO Index: Development of an Index for Monitoring and Prediction. Mon Weather Rev 132:1917–1932. https://doi.org/10.1175/1520-0493(2004)132<1917:AARMMI>2.0.CO;2

Wheeler MC, Hendon HH, Cleland S, Meinke H, Donald A (2009) Impacts of the Madden–Julian Oscillation on Australian Rainfall and Circulation. J Clim 22:1482–1498. https://doi.org/10.1175/2008JCLI2595.1

Wolding BO, Maloney ED (2015) Objective diagnostics and the Madden–Julian oscillation. Part I: Methodology. J Clim 28:4127–4140. https://doi.org/10.1175/JCLI-D-14-00688.1

Statements and Declarations

Funding: Support for this work was provided by (i) the Forewarned is Forearmed project (FWFA), which is supported by funding from the Australian Government Department of Agriculture as part of its Rural R&D for Profit programme, and (ii) Meat and Livestock Australia, the Queensland Government through the Drought and Climate Adaptation Program, and the University of Southern Queensland through the Northern Australia Climate Program (NACP). This research was undertaken with the assistance of resources from the National Computational Infrastructure Australia, a

National Collaborative Research Infrastructure Strategy enabled capability supported by the Australian Government.

Competing Interests: The authors have no relevant financial or non-financial interests to disclose.

Author Contributions: All authors contributed to the study conception and design. Material preparation, data collection and analysis were performed by Guomin Wang, Harry Hendon and Hai Lin. The first draft of the manuscript was written by Andrew Marshall and all authors commented on previous versions of the manuscript. All authors read and approved the final manuscript.

Data Availability: All observational and reanalysis data are publicly available. AWAP temperature data is available from https://doi.org/10.4227/166/5a8647d1c23e0., under the CC-BY-NC 4.0 International Licence. The MJO index data can be downloaded from http://www.bom.gov.au/climate/mjo/. ERAI data is available at https://apps.ecmwf.int/datasets/, and NOAA OLR data can be downloaded from https://psl.noaa.gov/data/gridded/data.interp_OLR.html. ACCESS-S1 retrospective forecast data is available to bona fide researchers upon request from the authors. The NCAR Command Language (NCL; https://www.ncl.ucar.edu) version 6.4.0 was used for data analysis and visualization of the results.